First-principles study of ferroelectric, dielectric, and piezoelectric properties in the nitride perovskites CeBN$_3$ (B = Nb, Ta)

Xian Zi,[1] Zunyi Deng,[1] Lixiang Rao,[1] Yongheng Li,[1] Gang Tang,[2,*] and Jiawang Hong ●[1,†]

[1]*School of Aerospace Engineering, Beijing Institute of Technology, Beijing 100081, China*
[2]*Advanced Research Institute of Multidisciplinary Science, Beijing Institute of Technology, Beijing 100081, China*

The nitride perovskite family has attracted widespread attention since the experimental synthesis of polar nitride perovskite LaWN$_3$. In this work, we investigated the ferroelectric, dielectric, and piezoelectric properties of two nitride perovskites CeBN$_3$ (B^{5+} = Nb, Ta) using the first-principles calculation. Our results show that the polarization values of CeNbN$_3$ (CNN) and CeTaN$_3$ (CTN) approach those of typical perovskites LiNbO$_3$ and BaTiO$_3$, respectively. Interestingly, the A-site cation contributes significantly to the polarization of CNN and CTN, despite the lack of lone pair electrons in Ce^{4+}. In addition, CTN and CNN exhibit unusually large static dielectric constants ($>$220) along the x direction, much larger than the y and z directions. This strong anisotropy primarily stems from the dominant infrared-active mode having a lower frequency or larger mode-effective charges along the x direction relative to the other two directions. Finally, we found both CTN and CNN have a comparatively large shear piezoelectric coefficient d_{24} over 70 pC/cm^2. Our research provides insights for understanding the origin of ferroelectricity in nitride perovskites and their potential piezoelectric applications.

I. INTRODUCTION

Perovskite semiconductors have attracted extensive research interest in numerous fields due to their widely tunable components and diverse properties [1–4]. For example, the ferroelectric [3,5], piezoelectric [6], magnetic [7], multiferroic [8], and superconducting [9] properties of oxide perovskites ABO$_3$ have led to their extensive research and application in many technological fields over the past century [3,10]. The excellent optoelectronic properties of halide perovskites ABX_3 (X = Cl, Br, I) make them ideal candidates for a variety of applications such as solar cells, light-emitting diodes, and detectors over the past decade [11–13]. Thus, the discovery of new types of perovskite materials will lead to a revolution in many fields, which is of great importance to the scientific and commercial communities.

In the last few years, many computational and experimental efforts have been devoted to the discovery of nitride perovskites, due to the importance of nitride semiconductors in the communication and information area [4,14–16]. For example, Sarmiento-Perez *et al.* screened 21 thermodynamically stable ABN$_3$, including LaReN$_3$, LaWN$_3$, and YReN$_3$, based on a combination of high-throughput techniques and global structural prediction methods [15]. Ha *et al.* predicted the two unknown metallic compounds CeWN$_3$ and CeMoN$_3$ using a thorough *ab initio* computational screening of ternary nitride perovskites [16]. Subsequently, Kloß *et al.* reported the preparation of a metallic nitride perovskite LaReN$_3$ through azide-mediated oxidation at high pressure [17]. And

Talley *et al.* successfully synthesized and characterized a polar nitride perovskite LaWN$_3$ with a large piezoelectric response (40 pm/V) [4]. Very recently, Sherbondy *et al.* experimentally realized two metallic nitride perovskites CeWN$_3$ and CeMoN$_3$ using subsequent thin film growth techniques [18]. It is noteworthy that the oxide states of cations are A^{3+} and B^{6+} in these experimentally reported ABN$_3$. Theoretical efforts have attempted to explore other combinations (e.g., A^{4+}/B^{5+}) of oxidation states to discover new nitride perovskites. For example, Ha *et al.* recently identified two compounds ABN$_3$ (A^{4+} = Ce and B^{5+} = Nb, Ta) with suitable band gaps through computational screening [16]. They systematically investigated the thermodynamical and dynamical stability, electronic properties, and optical absorption of CeTaN$_3$ (CTN) and CeNbN$_3$ (CNN), indicating their potential as solar cell absorbers. However, their other properties that are also critical for photovoltaic applications (e.g., dielectric constants, ferroelectric properties) are largely unknown at present.

In this work, we present a detailed study of the ferroelectric, dielectric, and piezoelectric properties of nitride perovskites CeBN$_3$ (B^{5+} = Nb, Ta) with polar symmetry using first-principles calculations. Our results show that the spontaneous polarization of CTN (CNN) is 29.18 (59.68) μC/cm^2. Interestingly, the A-site cation contributes significantly to the polarization of CNN and CTN, despite the absence of lone pair electrons in Ce^{4+}. In addition, we obtained the large static dielectric constant of CNN and CTN along the x direction of 226 and 381, respectively, much larger than the y and z directions. This pronounced anisotropy is primarily attributed to the fact that the dominant infrared-active mode exhibits a lower frequency or larger mode-effective charges along the x direction compared to the other two

*gtang@bit.edu.cn
†hongjw@bit.edu.cn

directions. Finally, we found that CTN and CNN have comparatively large shear piezoelectric coefficient d_{24} over 70 pC/cm^2, which is approximately 1.75 times greater than the experimentally measured d_{33} value of LaWN$_3$.

II. COMPUTATIONAL DETAILS

All calculations were carried out in the framework of density functional theory (DFT) as implemented in the Vienna Ab initio Simulation Package (VASP) code [19]. The electron exchange-correlation effects were chosen by the generalized gradient approximation (GGA) with Perdew-Burke-Ernzerhof functional (PBE) [20]. Since both CeNbN$_3$ and CeTaN$_3$ contain f-electron elements, we employed the HSE06 functional to calculate the density of states (DOS) [21,22]. Energy convergence can be further confirmed by using a cutoff energy of 520 eV. The k-point grid with a reciprocal space resolution of 0.02 Å^{-1} was employed for lattice optimization [23]. The lattice parameters and atomic positions were fully relaxed until the energy difference was less than 10^{-6} eV, and the force on each atom was smaller than 10^{-3} eV/Å. Chemical bonding analysis within the framework of the integrated crystal orbital bond index (ICOBI) was performed using LOBSTER [24–26]. The calculation of P_{ion} took into account the deviation of each ion in the unit cell from the centric reference phase and its rigid core's nominal charge. On the other hand, the electronic contribution P_{ele} was calculated using the Berry phase approach, which properly accounts for quantum effects [27]. The elastic constants C_{ij} discussed in the work below were calculated with finite differences implemented in the VASP code. The Voigt-Reuss-Hill approximation was used to estimate the bulk modulus, shear modulus, Young's modulus, and Poisson's ratio. The dielectric tensors and piezoelectric stress tensors were obtained using the density functional perturbation theory (DFPT) method [28]. The structures were visualized using VESTA software [29]. The Bilbao Crystallographic Server (BCS) was used for symmetry analysis [30–32].

III. RESULTS AND DISCUSSION

A. Structural properties and chemical bonding

First, we investigate the structural properties and chemical bonding characteristics of nitride perovskites CeBN$_3$ (B^{5+} = Nb, Ta). According to previous work [16], the paraelectric and ferroelectric structures of CeBN$_3$ belong to the orthorhombic phase with $Pnma$ (No. 62) and $Pmn2_1$ (No. 31) space group, respectively, as shown in Figs. 1(a) and 1(b). Through symmetry analysis, we decompose the atomic displacements associated with the $Pnma$-to-$Pmn2_1$ transition into the symmetry-adapted mode of the $Pnma$ phase, and the resulting mode is exclusively given by Γ_2^- [see Fig. 1(c)]. Examination of this Γ_2^- mode reveals that the dipole moment in CeBN$_3$ arises from the displacement of the Ce^{4+} cation, the B^{5+} cation, and the N^{3-} anion along different directions [see Figs. 1(d) and 1(e)]. It is notable that, in addition to the B-site cation and N^{3-} anion, meaningful displacement of the A-site Ce^{4+} cation is observed. The phonon spectra and phonon density of states (DOS) of $Pmn2_1$ phase CeBN$_3$, shown in Figs. S1 and S2 in the Supplemental Material [33], demonstrate the
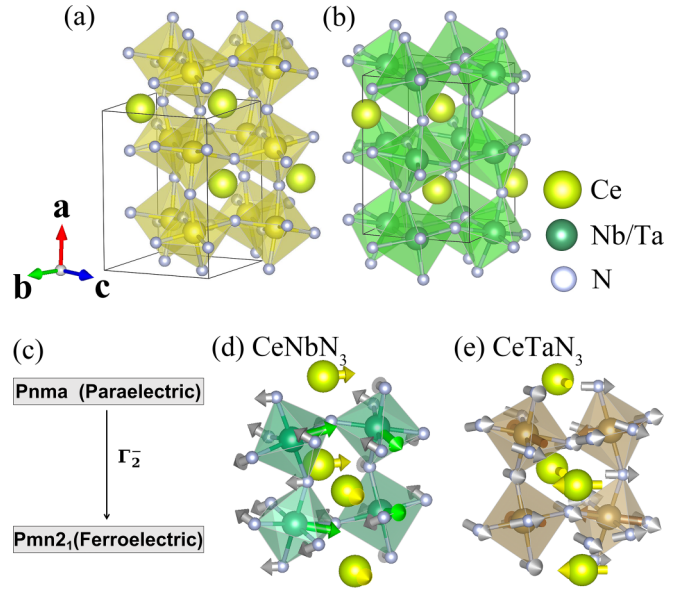
FIG. 1. (a) Centrosymmetric phase $Pnma$ and (b) ferroelectric phase $Pmn2_1$ of CeBN$_3$ (B = Nb, Ta). (c) The frame diagram of ferroelectric phase transition. Panels (d) and (e) show the Γ_2^- ferrodisplacive vibration modes for CNN and CTN, respectively.

structural stability at 0 K. In the phonon DOS of Figs. S1(b) and S1(d), the low frequencies near 0 THz mainly originate from vibrations of the Ce and B (B = Nb, Ta) atoms, while the high frequencies away from 5 THz mainly arise from the N atoms.

The optimized lattice parameters for the two phases of CeBN$_3$ are consistent with previous theoretical results [16], as listed in Table I. It can be found that the average bond length of Ta-N (2.09 Å) is shorter than that of Nb-N (2.12 Å) although the ionic radius of Ta^{5+} (0.6387 Å) is slightly larger than that of Nb^{5+} (0.6375 Å) [34]. The adjacent [BN_6] octahedra of CNN exhibit smaller $\angle_{B\text{-N-}B}$ bond angles (144.86°) than that of CTN (145.95°), the smaller $\angle_{B\text{-N-}B}$ angles indicate larger octahedron rotation in CNN. To further evaluate these distortions in CeBN$_3$, we introduce the quadratic elongation of bonds ($\langle\lambda\rangle$) and the variance of bond angles (σ^2), which can be defined by [35,36]

$$\langle\lambda\rangle = \frac{1}{6} \sum_{\{i=1\}}^{6} \left(\frac{d_i}{d_0}\right)^2, \tag{1}$$

$$\sigma^2 = \frac{1}{11} \sum_{\{i=1\}}^{12} (\alpha_i - 90)^2, \tag{2}$$

where d_i is the B-N bond length, d_0 is the mean B-N bond distance, and α_i is the N-B-N bond angle of the octahedra. The average $\langle\lambda\rangle$ and σ^2 of CeNbN$_3$ with the ferroelectric phase are calculated to be 1.00308 and 27.2 deg^2, respectively, which is higher than that of CeTaN$_3$ (1.00050 and 6.1 deg^2). A larger deviation of the value $\langle\lambda\rangle$ from 1 indicates a larger stretched or compressed octahedron, and a larger σ^2 indicates a higher deviation of B-site atom position from the center. The high deviation of the Nb^{5+}/Ta^{5+} ions, especially Nb^{5+} ions, from the [BN_6] octahedral center has an impact on the ferroelectric and piezoelectric properties discussed below.

TABLE I. Calculated structural parameters of ferroelectric ($Pmn2_1$) and paraelectric ($Pnma$) phases of CeBN$_3$ (B = Nb, Ta), including lattice constants $a/b/c$, volume V, average bond length d, average $\angle_{B\text{-N-}B}$ bond angle, average bond length quadratic elongation $\langle\lambda\rangle$, and average bond angle variance σ^2.

		a (Å)	b (Å)	c (Å)	V (Å^3)	$d_{B\text{-N}}$ (Å)	$\angle_{B\text{-N-}B}$ (deg)	$\langle\lambda\rangle$	σ^2 (deg^2)
	$Pmn2_1$	7.967	5.812	5.650	261.59	2.119	168.76	1.003 08	27.2
CNN	$Pmn2_1$ [16]	7.931	5.776	5.650	258.84	2.107	170.71		
	$Pnma$	7.972	5.734	5.607	256.14	2.091	173.01	1.000 04	2.0
	$Pmn2_1$	7.973	5.734	5.618	256.88	2.092	175.34	1.000 50	6.1
CTN	$Pmn2_1$ [16]	7.964	5.728	5.615	256.16	2.089	175.99		
	$Pnma$	7.792	5.736	5.607	255.67	2.086	176.95	1.000 02	1.7

To clarify the intrinsic chemical bonding characteristics in CeBN$_3$, we first calculate the electron localization function (ELF), as shown in Figs. 2(a) and 2(b). A low-ELF region (<0.5) can be found between the Ce and N ions in Figs. 2(a) and 2(b), suggesting there exists less covalent interaction on the Ce-N bonding. This also can be understood by the large differences in Pauli electronegativity for Ce (1.12) and N (3.04) atoms. Despite there existing a larger ELF between Nb (Ta) and N in CNN (CTN), they are still less than 0.5, revealing the low covalent level connecting the Nb (Ta) and N ions. We also calculate the integrated crystal orbital bond index (ICOBI) for CeBN$_3$, which is an intuitive method for quantifying covalent bonding in solid-state materials [24,25]. As shown in Figs. 2(c) and 2(d) the ICOBI values for Nb-N (0.708) bonds in CNN and Ta-N (0.672) bonds in CTN further confirm the coexistence of ionicity and covalency, meanwhile, ICOBI values for Ce-N bonds in CNN and CTN suggest the less covalent components. These values also indicate that the

Nb-N bonding in CNN is stronger than the Ta-N bonding in CTN.

B. Ferroelectric properties

To assess the ferroelectric properties, we employed the PSEUDO tool from the Bilbao Crystallographic Server [30–32] to generate four centrosymmetric reference structures: $Pmna$, $Pnnm$, $Pmmn$, and $Pnma$, using the low-symmetry $Pmn2_1$ structure as the starting point. Among these, the $Pnma$ structure showed the smallest atomic displacement relative to the ferroelectric $Pmn2_1$ structure, shown in Fig. S3 in Supplemental Material [33]. Figure 3 shows the total spontaneous polarization ($P_{\text{tot}} = P_{\text{ion}} + P_{\text{ele}}$) of Ce$BN_3$ (B = Nb, Ta) along the path from the $-Pnm2_1$ structure ($x = -1$) to the paraelectric $Pnma$ phase ($x = 0$) to the ferroelectric $Pmn2_1$ phase ($x = 1$), as calculated using the Berry phase method [37]. The ionic (P_{ion}) and electronic (P_{ele}), and total contributions (P_{tot}) are also plotted in Fig. 3 and S4. The total polarization along the [001] direction is 59.68 μC/cm^2 for CNN and 29.18 μC/cm^2 for CTN. The electronic and ionic contributions are in opposite directions, with the magnitude of the ionic contribution being significantly larger than that of the electronic contribution. The estimated polarization value of CNN is close to that of the $R3c$ phase LaWN$_3$ (52–84 μC/cm^2) [14,15] and the $R3c$ phase LiNbO$_3$ (62–76 μC/cm^2) [38]. Meanwhile, the polarization value of CTN is comparable to that of the $Pna2_1$ phase LaWN$_3$ (20 μC/cm^2) [14] and traditional BaTiO$_3$ ($\sim$25 μC/cm^2) [28]. To understand the origin of the spontaneous polarization in the two
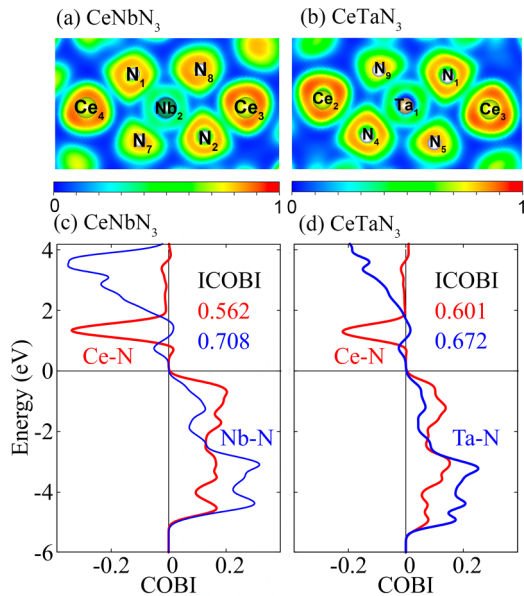
FIG. 2. Two-dimensional schematic diagram of the electron localization function (ELF) for (a) CeNbN$_3$ (the plane including Ce3, Nb2, and N2 atoms is selected) and (b) CeTaN$_3$ (the plane including Ce3, Ta1, and N5 atoms is selected). The isosurface level is 0.90e/bohr^3. (c), (d) Crystal orbital bond indices (COBIs) of the selected shortest Ce-N interactions and B-N (B = Nb, Ta) interactions of the $Pmn2_1$ phase of CeNbN$_3$ and CeTaN$_3$.
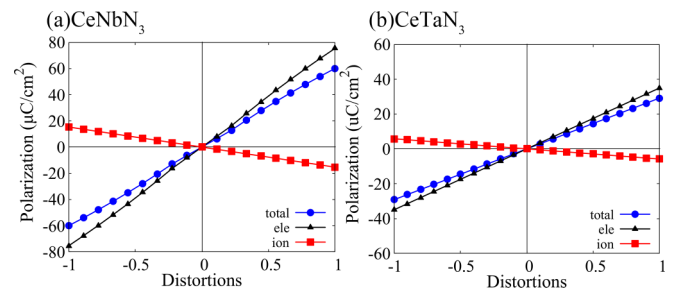
FIG. 3. The calculated polarization values of (a) CNN and (b) CTN along the path from the $-Pnm2_1$ structure ($x = -1$) to the paraelectric $Pnma$ phase ($x = 0$) to the ferroelectric $Pmn2_1$ phase ($x = 1$). The displacement from the paraelectric $Pnma$ phase ($x = 0$) to the ferroelectric $Pmn2_1$ phase ($x = 1$) is normalized to 1.

TABLE II. The calculated Born effective charges of the $Pmn2_1$ phase of CeBN$_3$ (B = Nb, Ta). The serial number of different elements represents the Wyckoff positions.

	Z^*_{11}	Z^*_{22}	Z^*_{33}		Z^*_{11}	Z^*_{22}	Z^*_{33}
Ce-1	5.73	4.98	7.16	Ce-1	6.41	6.65	6.31
Ce-2	6.24	7.10	5.56	Ce-2	6.11	5.86	7.09
Nb-1	8.77	8.35	7.00	Ta-1	8.95	9.22	8.59
N-1	−8.02	−3.23	−3.20	N-1	−6.71	−3.97	−5.09
N-2	−6.17	−3.86	−5.06	N-2	−7.46	−3.83	−4.30
N-3	−3.74	−5.06	−4.90	N-3	−4.10	−5.94	−5.14
N-4	−3.92	−5.78	−4.33	N-4	−4.02	−5.63	−5.45

nitride perovskites, we listed the Born effective charges of CeBN$_3$ in Table II. It is evident that the Z^* values differ substantially from the nominal charge (+4 for Ce, +5 for Nb and Ta, and −3 for N). In particular, the anomalously large Z^* values for the B-site metal cations emphasize their significant role as the driving force behind the ferroelectric distortion.

To further elucidate the origins of the ferroelectric polarizations in CeBN$_3$, the energy gains of partial distortion modes [Ce + N, Nb(Ta) + N, Ce + Nb(Ta)] were calculated with HSE, as compared in Fig. 4. These partial distortion modes represent the displacements of only selected ions, while the full mode denotes displacements of all ions. For CNN, similar double-well energy profiles are observed for the partial Nb + N and Ce + N modes, although the former is shallower than the latter. These dual double-well profiles imply that not only does the Nb-N orbital hybridization contributes to its polarization, but the Ce and Nb ion pairs also have prominent contribution. In contrast, for CTN, only the double-well energy profile is observed for the partial Ce + Ta mode, implying that the Ce and Ta ion pairs are the only contributors to the polarization. This observed phenomenon of significant
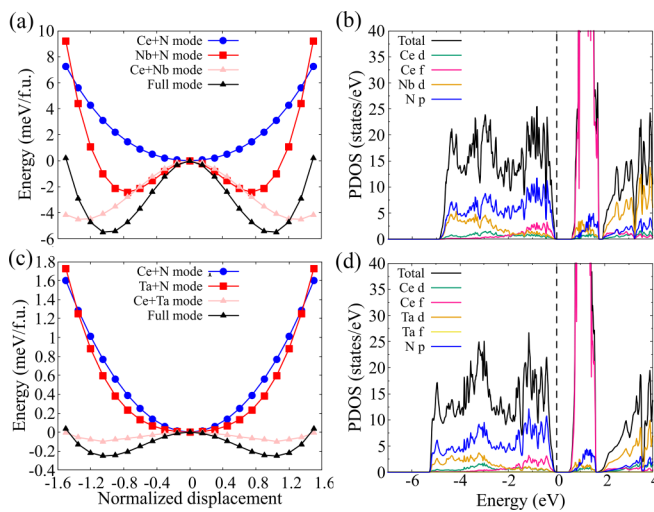
FIG. 4. Double-well energy profiles as a function of normalized displacement for the full mode and partial modes of (a) CeNbN$_3$ and (c) CeTaN$_3$. The ferroelectric $Pmn2_1$ phase is set at 1 and the paraelectric $Pnma$ phase is set at 0. The total and projected density of states (DOS) calculated using HSE06 for (b) CeNbN$_3$ and (d) CeTaN$_3$.

contributions from the Ce + Nb(Ta) ion pairs is markedly different from previous reports on LaWN$_3$ (mainly W + N mode) and GdWN$_3$ (mainly W + N and Gd + N modes) [39]. The calculated partial density of states (PDOS) with HSE in Figs. 4(b) and 4(d) and the comparison of HSE and SCAN of CeTaN$_3$ as showed in Fig. S5 also show that the Ce f orbitals and Nb/Ta d orbitals make meaningful contributions to the band edges.

C. Dielectric properties

The static dielectric constants (ε_{st}) of solids consist of electronic (ε_∞) and ionic (ε_{ion}) contributions. The calculated values for ε_{st}, ε_∞, and ε_{ion} of CeBN$_3$ (B = Nb, Ta) along the x, y, and z directions are shown in Table III. The values of ε_{st}^{xx}, ε_{st}^{yy}, and ε_{st}^{zz} for CNN (CTN) are 226.19 (381.20), 106.55 (226.94), and 97.83 (259.96), respectively. Such large values of ε_{st} in CeBN$_3$ imply their potential for effective screening of defects and impurities, which is beneficial for carrier transport properties. This is very advantageous for photovoltaic applications of these materials. In addition, it is noteworthy that the orthorhombic phase of CeBN$_3$ displays significant anisotropy in their dielectric constants across different crystallographic directions. The strong anisotropy in the dielectric constants arises primarily from anisotropic ionic contributions, while the electronic contributions show little directional dependence. Specifically, the ionic dielectric constant along the x axis of CNN (CTN) is 197.97 (360.35), markedly higher than the values along the y and z axes.

To elucidate the strong anisotropy in the ionic contributions along different directions, the contribution of each infrared (IR) active phonon mode λ to the total ionic dielectric response can be obtained from the following formula [40–42]:

$$\epsilon_{\alpha\beta}^{ion} = \frac{4\pi e^2}{M_0 V} \sum_\lambda \frac{\tilde{Z}^*_{\lambda\alpha} \tilde{Z}^*_{\lambda\beta}}{\omega_\lambda^2}, \tag{3}$$

where M_0 is a reference mass, V is the volume of a unit cell, ω_λ is the infrared active phonon frequency, and $\tilde{Z}^*_{\lambda\alpha}$ is the mode effective charge tensors. $\tilde{Z}^*_{\lambda\alpha}$ can be obtained by the formula $\tilde{Z}^*_{\lambda\alpha} = \sum_{i\beta} Z^*_{i,\alpha\beta} (\frac{M_0}{M_i})^{1/2} \xi_{i,\lambda\beta}$, where $\xi_{i,\lambda\beta}$ is the eigendisplacement of atom i in phonon mode λ [43]. Therefore, a large ionic contribution could arise from factors such as low-frequency IR-active phonons, large mode-effective charges, or an increased number of IR-active modes.

CeBN$_3$ (B = Nb, Ta) in the $Pmn2_1$ phase possesses a total of 60 mechanical vibration modes. Among these, the 57 optical modes at the Brillouin-zone center are characterized by irreducible representations, namely, A_1, A_2, B_1, and B_2 modes.

$$\Gamma_{opt} = 16A_1 \oplus 13A_2 \oplus 12B_1 \oplus 16B_2. \tag{4}$$

The IR modes contributing to the ionic dielectric constants are A_1, B_1, and B_2, with respective counts of 16, 12, and 16. Consequently, both CNN and CTN exhibit a total of 44 IR-active modes. For each IR mode λ, the ω_λ, $\tilde{Z}^*_\lambda$, and $\epsilon_{\lambda,\alpha\beta}$ are listed in Tables S1 and S2 in the Supplemental Material [33]. The contributions of the IR-active phonon modes ($\omega_\lambda < 18$ THz) to the ionic part of the dielectric tensor and the corresponding mode-effective charges along different crystallographic directions are shown in Fig. 5.

TABLE III. Ionic contribution (ε_{ion}) and electronic contribution (ε_{ele}) to the static dielectric constants ($\varepsilon_{st} = \varepsilon_{ele} + \varepsilon_{ion}$) of the $Pmn2_1$ phase of CeBN$_3$ (B = Nb, Ta). Literature values for the band gaps of CeBN$_3$ in eV are also provided. ε_{ion} originates from the displacement of ionic core positions under an external field, while ε_{ele} arises from the polarization of electron clouds.

	ε_{ion}^{xx}	ε_{ion}^{yy}	ε_{ion}^{zz}	$\varepsilon_{\infty}^{xx}$	$\varepsilon_{\infty}^{yy}$	$\varepsilon_{\infty}^{zz}$	ε_{st}^{xx}	ε_{st}^{yy}	ε_{st}^{zz}	E_g
CNN	197.97	79.31	71.37	28.22	27.25	26.46	226.19	106.55	97.83	1.90 [4]
CTN	360.35	204.00	239.84	20.85	22.93	20.12	381.20	226.94	259.96	1.73 [4]

According to Fig. 5, Tables S1 and S2 in the Supplemental Material [33], for CNN, the dominant IR-active phonon modes along the x, y, and z axes have frequencies of 3.77, 7.59, and 3.96 THz, with corresponding mode-effective charges of $-2.79e$, $3.14e$, and $-1.45e$, respectively. As we can see from Fig. 5 and Table S3 in the Supplemental Material [33], the much higher ε_{ion}^{xx} compared to ε_{ion}^{yy} in CNN is mainly attributed to the lower frequency (i.e., 3.77 THz for ε_{ion}^{xx} and 7.59 THz for ε_{ion}^{yy}) of the IR-active mode that contributes the most to the ionic dielectric response. However, this alone cannot explain why ε_{ion}^{xx} is much higher than ε_{ion}^{zz}, since the lowest frequencies along these two directions are very close (i.e., 3.77 THz for ε_{ion}^{xx} and 3.96 THz for ε_{ion}^{zz}). Furthermore, the absolute value of the mode-effective charge corresponding to the lowest frequency along the x direction ($-2.79e$) is larger than that along the z direction ($-1.45e$), which plays an important role in making the ionic dielectric constant much higher along the x direction than the z direction. In addition, the second largest contributing IR-active modes to the ionic dielectric response along the x direction have lower frequencies and larger mode-effective charges, which have an important contribution as well (see Table S3 in the Supplemental Material [33]).

Similarly, for CTN, the dominant IR-active phonon modes along the x, y, and z directions have frequencies of 3.08, 5.09, and 1.62 THz, with corresponding mode-effective charges of $-3.54e$, $-3.32e$, and $-1.65e$, respectively. From Fig. 5 and Table S3 in the Supplemental Material [33], it can be seen that the much higher ε_{ion}^{xx} compared to ε_{ion}^{yy} in CNN can primarily be attributed to the fact that the dominant IR-active mode has a

lower frequency (i.e., 3.08 THz for ε_{ion}^{xx} and 5.09 THz for ε_{ion}^{yy}). On the other hand, the substantial difference between ε_{ion}^{xx} and ε_{ion}^{zz} in CTN is mainly due to the dominant IR-active mode having a larger absolute value of the mode-effective charge (i.e., $-3.54e$ for ε_{ion}^{xx} and $-1.65e$ for ε_{ion}^{zz}).

D. Mechanical properties

Mechanical properties are of critical importance for many practical applications [44,45]. We calculated the elastic stiffness tensor C_{ij} of CeBN$_3$ (B = Nb, Ta), as presented in Table IV. Due to their orthorhombic symmetry ($Pmn2_1$ space group), nine independent elastic constants were obtained for CNN and CTN. Based on the Born criteria for mechanical stability [46], both CNN and CTN were found to be mechanically stable. The calculated C_{11}, C_{12}, and C_{33} for the two compounds are larger than 300 GPa, indicating strong incompressibility along the a, b, and c axis, respectively. The C_{11} value exceeds C_{33} in CTN, reflecting greater resistance to deformation along the a axis versus the c axis. Conversely, CNN exhibits higher C_{33} over C_{11}, indicating stronger resistance along the c axis than the a axis. It is worth noting that C_{44}/C_{55} of CTN/CNN is the smallest among the nine elastic constants, indicating weak resistance to shear in the (001)/(100) plane. In addition, it can be seen that the elastic constants of CeBN$_3$ are slightly larger than that of the analogous LaWN$_3$ compound ($R3c$ space group) [47], but the elastic constants of nitride perovskite are much larger than those of typical oxide (i.e., PbTiO$_3$) and halide perovskites (i.e., CsPbI$_3$) [48]. The
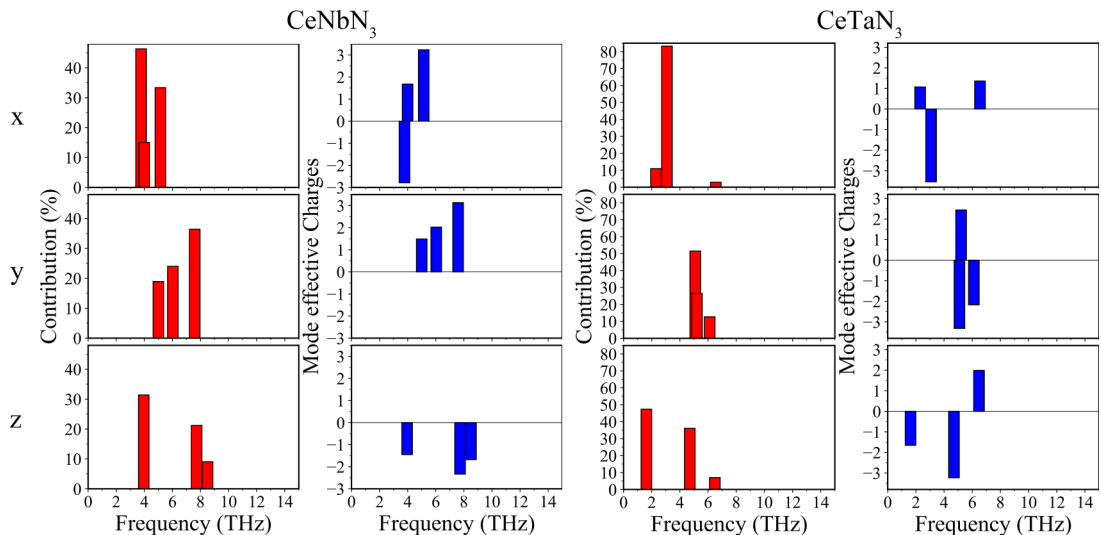
FIG. 5. Mode contribution (%) and mode effective charges along the $x/y/z$ direction to the ionic dielectric constants for the $Pmn2_1$ phase of CNN and CTN. For simplicity and clarity, the top three contributions and corresponding mode effective charges are shown here, the detailed data are shown in Tables S1 and S2 in Supplemental Material [33].

TABLE IV. Elastic stiffness tensor C_{ij}, mechanical moduli (GPa), and hardness of the $Pmn2_1$ phase of $CeBN_3$ (B = Nb, Ta), and the data of LaWN$_3$ ($R3c$), PbTiO$_3$ ($P4mm$), and CsPbI$_3$ ($Pm\bar{3}m$) are listed for comparison. The data of PbTiO$_3$ ($P4mm$) was calculated with the same computing environment as CTN and CNN.

	CTN	CNN	LaWN$_3$ [47]	PbTiO$_3$	CsPbI$_3$ [48]
C_{11}	395.42	376.10	327.80	235	26.07
C_{22}	321.25	387.74	243.53	235	32.02
C_{33}	335.18	388.53	323.84	105	13.77
C_{44}	97.52	117.81	95.52	65	4.61
C_{55}	117.67	116.29	109.23	65	11.20
C_{66}	131.93	128.18	63.73	104	5.97
C_{12}	138.05	130.48	81.95	101	8.51
C_{13}	147.17	135.16	139.81	99	13.78
C_{23}	132.98	136.51	81.95	99	9.51
Bulk modulus B	208.77	217.37	169.56	101.80	14.07
Young's modulus E	309.12	282.47	202.04	147.07	15.67
Shear modulus G	110.82	122.38	77.62	58.40	5.96
Poisson's ratio ν	0.27	0.26	0.37	0.26	0.31
Hardness Hv	2.95	2.76			
B/G	1.88	1.78	2.18	1.74	2.36

mechanical moduli, including bulk modulus (B), shear modulus (G), and Young's modulus (E), show the same trend. This may be attributed to the fact that nitrogen has high chemical hardness and intermediate electronegativity, which allows it to form strong metal-nitride bonding [49]. Pugh's ratio B/G and Poisson's ratio ν are usually used to evaluate the brittle or ductile behavior of solid materials [50,51]. If the value of B/G is greater than 1.75 or ν is greater than 2/7, then the solid is flexible; otherwise, it is brittle [52,53]. According to this criterion, the two nitride perovskites are all ductile, despite the high hardness of the nitrogen element.

To understand the directional dependence of elastic properties, we derived the directional dependence of Young's moduli and Poisson's ratios for $CeBN_3$ with respect to different crystallographic directions [54], as displayed in Fig. 6. It can be seen that CTN exhibits almost isotropic Young's moduli and Poisson's ratios along the three crystal planes. For

CNN, Young's moduli and Poisson's ratios projections on the (100) and (010) planes show almost similar isotropic behavior. However, Young's modulus (Poisson's ratio) projected on the (001) plane is anisotropic and reaches a maximum value at $0°$ ($45°$) or $90°$ ($135°$).

E. Piezoelectric properties

Based on the crystal point group ($mm2$) of $CeBN_3$ (B = Nb, Ta), the piezoelectric stress tensor has five independent elements, namely e_{31}, e_{32}, e_{33}, e_{24}, and e_{15}. Indeed, the piezoelectric tensor can be written as

$$e_{ij} = \begin{bmatrix} 0 & 0 & 0 & 0 & e_{15} & 0 \\ 0 & 0 & 0 & e_{24} & 0 & 0 \\ e_{31} & e_{32} & e_{33} & 0 & 0 & 0 \end{bmatrix}. \quad (5)$$

The calculated values for these five elements are presented in Table V. First, it can be seen that the five piezoelectric stress constants for CNN are all positive, while those for CTN are all negative. This is due to the dominant internal-strain piezoelectric stress coefficients being positive in CNN, but negative in CTN (see Table S4 in the Supplemental Material [33]). The piezoelectric strain coefficients of $CeBN_3$ can be attained through the formula $d_{ij} = \sum_{k=1}^{6} e_{ik} S_{kj}$ [55] (see Table V), where S_{kj} represents the elastic compliance matrix $[S_{kj} = (C_{kj})^{-1}]$. The piezoelectric strain component

FIG. 6. Two-dimensional (2D) projection in polar coordinates in the (a), (d) (001), (b), (e) (010), and (c), (f) (100) planes of Young's modulus E (the upper plane) and Poisson's ratio ν (the bottom plane) of the $Pmn2_1$ phase of CTN (red) and CNN (blue).

TABLE V. The calculated piezoelectric stress and strain tensors for the $Pmn2_1$ phase of $CeBN_3$ (B = Nb, Ta).

Index (ij)	CNN e_{ij} (C/m^2)	CNN d_{ij} (pC/N)	CTN e_{ij} (C/m^2)	CTN d_{ij} (pC/N)
31	1.98	−4.05	−1.24	12.52
32	4.11	11.03	−7.80	−20.06
33	5.04	15.72	−8.61	−23.21
24	4.56	78.41	−6.85	−70.23
15	1.57	15.59	−0.76	−6.47

with the largest absolute value for both CNN and CTN was d_{24}, exhibiting values of 78.41 and 70.23 pC/N, respectively. According to the relationship $d_{24} = e_{24} \times S_{44}$, the notably high d_{24} likely arises predominantly from the large S_{44}. As discussed in the preceding section on mechanical properties, it was found that C_{44} was relatively small compared to the other elastic constants in both CNN and CTN. Compared to prototypical inorganic perovskite oxides such as $BaTiO_3$ ($d_{15} = 270$ pC/N) [56], the shear piezoelectric coefficients in CeBN$_3$ are smaller. However, they are much larger than those for common inorganic crystals such as LiTaO$_3$ ($d_{15} = 26$ pC/N) [57] and CdS ($d_{15} = -14$ pC/N) [58].

In terms of applications, the electromechanical coupling coefficient k_{ij} represents the effectiveness of energy conversion for piezoelectrics. The coupling coefficient is calculated as $k_{ij} = \frac{d_{ij}}{\sqrt{\varepsilon_{ii} S_{jj}}}$, where the ε_{ii} is the staic dielectric constant. Interestingly, the computed electromechanical coupling coefficients (for CNN, $k_{24} = 0.47$; and for CTN, $k_{24} = 0.41$) are comparable to those of typical inorganic piezoelectrics like ZnO ($k_{33} = 0.41$) [58] and BaTiO$_3$ ($k_{33} = 0.42$) [59]. Our results demonstrate that CeBN$_3$ (B = Nb, Ta) exhibits a large piezoelectric response and is a promising candidate material for various piezoelectric applications.

IV. CONCLUSION

In summary, we have investigated the ferroelectric, dielectric, and piezoelectric properties of CeBN$_3$ (B^{4+} = Nb, Ta) with $Pmn2_1$ space group using first-principles calculations. Our results show that the spontaneous polarization of CTN and CNN is 29.18 and 59.68 μC/cm^2, respectively,

approaching those of typical perovskite LiNbO$_3$ (62–76 μC/cm^2) and BaTiO$_3$ ($\sim$25 μC/cm^2). Interestingly, the A-site contributes significantly to the polarization of CNN and CTN, despite Ce^{4+} lacking lone pair electrons. Additionally, we obtained the large static dielectric constant of CNN and CTN along the x direction as 226 and 381, respectively, much larger than the y and z directions. This pronounced anisotropy primarily arises from the fact that the dominant infrared-active mode exhibits a lower frequency or larger mode-effective charges along the x direction compared to the other two directions. We found that CNN and CTN have comparatively large shear piezoelectric coefficients d_{24} of 78.41 and -70.23 pC/cm^2, respectively. These d_{24} values are approximately 1.75 times greater than the experimentally measured d_{33} value of LaWN$_3$. This is attributed to the relatively small C_{44} values in CNN and CTN. Moreover, the estimated electromechanical coupling coefficients for CNN and CTN are over 0.41. Our results reveal that nitride perovskite has the potential for application in the field of ferroelectricity and piezoelectricity as a multifunctional material and opens a different avenue to explore nitride semiconductors.

[1] S. P. Beckman, X. Wang, K. M. Rabe, and D. Vanderbilt, Ideal barriers to polarization reversal and domain-wall motion in strained ferroelectric thin films, Phys. Rev. B **79**, 144124 (2009).

[2] S. E. Reyes-Lillo and K. M. Rabe, Antiferroelectricity and ferroelectricity in epitaxially strained PbZrO$_3$ from first principles, Phys. Rev. B **88**, 180102(R) (2013).

[3] W. Gao, Y. Zhu, Y. Wang, G. Yuan, and J.-M. Liu, A review of flexible perovskite oxide ferroelectric films and their application, J. Materiomics **6**, 1 (2020).

[4] K. R. Talley, C. L. Perkins, D. R. Diercks, G. L. Brennecka, and A. Zakutayev, Synthesis of LaWN$_3$ nitride perovskite with polar symmetry, Science **374**, 1488 (2021).

[5] J. F. Scott and M. Dawber, Oxygen-vacancy ordering as a fatigue mechanism in perovskite ferroelectrics, Appl. Phys. Lett. **76**, 3801 (2000).

[6] Y. Bai, T. Siponkoski, J. Peräntie, H. Jantunen, and J. Juuti, Ferroelectric, pyroelectric, and piezoelectric properties of a photovoltaic perovskite oxide, Appl. Phys. Lett. **110**, 063903 (2017).

[7] J. He, A. Borisevich, S. V. Kalinin, S. J. Pennycook, and S. T. Pantelides, Control of octahedral tilts and magnetic properties of perovskite oxide heterostructures by substrate symmetry, Phys. Rev. Lett. **105**, 227203 (2010).

[8] H. Liu and X. Yang, A brief review on perovskite multiferroics, Ferroelectrics **507**, 69 (2017).

[9] A. W. Sleight, J. L. Gillson, and P. E. Bierstedt, High-temperature superconductivity in the BaPb$_{1-x}$Bi$_x$O$_3$ systems, Solid State Commun. **17**, 27 (1975).

[10] C. Sun, J. A. Alonso, and J. Bian, Recent advances in perovskite-type oxides for energy conversion and storage applications, Adv. Energy Mater. **11**, 2000459 (2021).

[11] W.-J. Yin, J.-H. Yang, J. Kang, Y. Yan, and S.-H. Wei, Halide perovskite materials for solar cells: a theoretical review, J. Mater. Chem. A **3**, 8926 (2015).

[12] X.-K. Liu, W. Xu, S. Bai, Y. Jin, J. Wang, R. H. Friend, and F. Gao, Metal halide perovskites for light-emitting diodes, Nat. Mater. **20**, 10 (2021).

[13] Z. Li, F. Zhou, H. Yao, Z. Ci, Z. Yang, and Z. Jin, Halide perovskites for high-performance X-ray detector, Mater. Today **48**, 155 (2021).

[14] Y.-W. Fang, C. A. J. Fisher, A. Kuwabara, X.-W. Shen, T. Ogawa, H. Moriwake, R. Huang, and C.-G. Duan, Lattice dynamics and ferroelectric properties of the nitride perovskite LaWN$_3$, Phys. Rev. B **95**, 014111 (2017).

[15] R. Sarmiento-Pérez, T. F. T. Cerqueira, S. Körbel, S. Botti, and M. A. L. Marques, Prediction of stable nitride perovskites, Chem. Mater. **27**, 5957 (2015).

[16] V.-A. Ha, H. Lee, and F. Giustino, CeTaN$_3$ and CeNbN$_3$: Prospective Nitride Perovskites with Optimal Photovoltaic Band Gaps, Chem. Mater. **34**, 2107 (2022).

[17] S. D. Kloß, M. L. Weidemann, and J. P. Attfield, Preparation of bulk-phase nitride perovskite LaReN$_3$ and topotactic reduction to LaNiO$_2$-Type LaReN$_2$, Angew. Chem. Int. Ed. **60**, 22260 (2021).

[18] R. Sherbondy, R. W. Smaha, C. J. Bartel, M. E. Holtz, K. R. Talley, B. Levy-Wendt, C. L. Perkins, S. Eley, A. Zakutayev, and G. L. Brennecka, High-throughput selection and experimental realization of two new Ce-based nitride perovskites: CeMoN$_3$ and CeWN$_3$, Chem. Mater. **34**, 6883 (2022).

[19] G. Kresse and J. Furthmüller, Efficient iterative schemes for *ab initio* total-energy calculations using a plane-wave basis set, Phys. Rev. B **54**, 11169 (1996).

[20] J. P. Perdew, K. Burke, and M. Ernzerhof, Generalized gradient approximation made simple, Phys. Rev. Lett. **77**, 3865 (1996).

[21] J. Heyd and G. E. Scuseria, Efficient hybrid density functional calculations in solids: Assessment of the Heyd–Scuseria–Ernzerhof screened Coulomb hybrid functional, J. Chem. Phys. **121**, 1187 (2004).

[22] J. Heyd, G. E. Scuseria, and M. Ernzerhof, Hybrid functionals based on a screened Coulomb potential, J. Chem. Phys. **118**, 8207 (2003).

[23] P. E. Blöchl, O. Jepsen, and O. K. Andersen, Improved tetrahedron method for Brillouin-zone integrations, Phys. Rev. B **49**, 16223 (1994).

[24] R. Dronskowski and P. E. Blöchl, Crystal orbital Hamilton populations (COHP): energy-resolved visualization of chemical bonding in solids based on density-functional calculations, J. Phys. Chem. **97**, 8617 (1993).

[25] P. C. Müller, C. Ertural, J. Hempelmann, and R. Dronskowski, Crystal orbital bond index: covalent bond orders in solids, J. Phys. Chem. C **125**, 7959 (2021).

[26] S. Maintz, V. L. Deringer, A. L. Tchougréeff, and R. Dronskowski, LOBSTER: A tool to extract chemical bonding from plane-wave based DFT (Wiley Online Library, 2016).

[27] R. D. King-Smith and D. Vanderbilt, Theory of polarization of crystalline solids, Phys. Rev. B **47**, 1651(R) (1993).

[28] X. Wu, D. Vanderbilt, and D. R. Hamann, Systematic treatment of displacements, strains, and electric fields in density-functional perturbation theory, Phys. Rev. B **72**, 035105 (2005).

[29] K. Momma and F. Izumi, VESTA: A three-dimensional visualization system for electronic and structural analysis, J. Appl. Crystallogr. **41**, 653 (2008).

[30] E. Kroumova, M. I. Aroyo, J. M. Perez-Mato, S. Ivantchev, J. M. Igartua, and H. Wondratschek, PSEUDO: A program for a pseudo-symmetry search, J. Appl. Crystallogr. **34**, 783 (2001).

[31] C. Capillas, M. I. Aroyo, and J. M. Perez-Mato, Methods for pseudosymmetry evaluation: A comparison between the atomic displacements and electron density approaches, Z. Krist. Cryst. Mater. **220**, 691 (2005).

[32] C. Capillas, E. S. Tasci, G. de la Flor, D. Orobengoa, J. M. Perez-Mato, and M. I. Aroyo, A new computer tool at the Bilbao Crystallographic Server to detect and characterize pseudosymmetry, Z. Krist. Cryst. Mater. **226**, 186 (2011).

[33] See Supplemental Material at http://link.aps.org/supplemental/10.1103/PhysRevB.109.115125 for phonon spectra, density of states (DOS) of CeTaN$_3$ and CeNbN$_3$, the phonon spectra with

out and without LO-TO splitting, the scalar mode effective charge along the $x/y/z$ directions, the total dielectric constants and the dielectric components along the $x/y/z$ directions for each IR-active mode, the top three dielectric contributions (%) along the x, y, and z directions and corresponding IR-active modes and mode effective charge components of CNN and CTN, internal-strain and clamped-ion piezoelectric stress coefficients, calculated polarization as a function of distortion from the $-Pnm2_1$ structure to the $Pnm2_1$ structure, the comparison of the total and projected DOS calculated using HSE and SCAN functionals.

[34] A. A. B. Baloch, S. M. Alqahtani, F. Mumtaz, A. H. Muqaibel, S. N. Rashkeev, and F. H. Alharbi, Extending Shannon's ionic radii database using machine learning, Phys. Rev. Mater. **5**, 043804 (2021).

[35] K. Du, Q. Tu, X. Zhang, Q. Han, J. Liu, S. Zauscher, and D. B. Mitzi, Two-dimensional lead(II) halide-based hybrid perovskites templated by acene alkylamines: Crystal structures, optical properties, and piezoelectricity, Inorg. Chem. **56**, 9291 (2017).

[36] K. Robinson, G. V. Gibbs, and P. H. Ribbe, Quadratic elongation: A quantitative measure of distortion in coordination polyhedra, Science **172**, 567 (1971).

[37] D. Xiao, M.-C. Chang, and Q. Niu, Berry phase effects on electronic properties, Rev. Mod. Phys. **82**, 1959 (2010).

[38] C. Ederer and N. A. Spaldin, Effect of epitaxial strain on the spontaneous polarization of thin film ferroelectrics, Phys. Rev. Lett. **95**, 257601 (2005).

[39] C. Gui, J. Chen, and S. Dong, Multiferroic nitride perovskites with giant polarizations and large magnetic moments, Phys. Rev. B **106**, 184418 (2022).

[40] X. Zhao and D. Vanderbilt, First-principles study of structural, vibrational, and lattice dielectric properties of hafnium oxide, Phys. Rev. B **65**, 233106 (2002).

[41] N. Ashkenov, B. N. Mbenkum, C. Bundesmann, V. Riede, M. Lorenz, D. Spemann, E. M. Kaidashev, A. Kasic, M. Schubert, M. Grundmann *et al.*, Infrared dielectric functions and phonon modes of high-quality ZnO films, J. Appl. Phys. **93**, 126 (2003).

[42] J. W. Bennett, I. Grinberg, and A. M. Rappe, Effect of substituting of S for O: The sulfide perovskite BaZrS$_3$ investigated with density functional theory, Phys. Rev. B **79**, 235115 (2009).

[43] X. Zhao and D. Vanderbilt, Phonons and lattice dielectric properties of zirconia, Phys. Rev. B **65**, 075105 (2002).

[44] L.-J. Ji, S.-J. Sun, Y. Qin, K. Li, and W. Li, Mechanical properties of hybrid organic-inorganic perovskites, Coord. Chem. Rev. **391**, 15 (2019).

[45] D. Yang, R. Yang, S. Priya, and S. Liu, Recent advances in flexible perovskite solar cells: Fabrication and applications, Angew. Chem. Int. Ed. **58**, 4466 (2019).

[46] M. Born, On the stability of crystal lattices, Math. Proc. Camb. Philos. Soc. **36**, 160 (1940).

[47] X. Liu, J. Fu, and G. Chen, First-principles calculations of electronic structure and optical and elastic properties of the novel ABX$_3$-type LaWN$_3$ perovskite structure, RSC Adv. **10**, 17317 (2020).

[48] S. Li, S. Zhao, H. Chu, Y. Gao, P. Lv, V. Wang, G. Tang, and J. Hong, Unraveling the factors affecting the mechanical properties of halide perovskites from first-principles calculations, J. Phys. Chem. C **126**, 4715 (2022).

[49] W. T. Zheng and C. Q. Sun, Electronic process of nitriding: Mechanism and applications, Prog. Solid State Chem. **34**, 1 (2006).

[50] S. F. Pugh, XCII. Relations between the elastic moduli and the plastic properties of polycrystalline pure metals, Lond. Edinb. Dublin Philos. Mag. J. Sci. **45**, 823 (1954).

[51] N. A. Noor, S. M. Alay-e-Abbas, M. Hassan, I. Mahmood, Z. A. Alahmed, and A. H. Reshak, The under-pressure behaviour of mechanical, electronic and optical properties of calcium titanate and its ground state thermoelectric response, Philos. Mag. **97**, 1884 (2017).

[52] J. Cao and F. Li, Critical Poisson's ratio between toughness and brittleness, Philos. Mag. Lett. **96**, 425 (2016).

[53] M. L. Ali and M. Z. Rahaman, Investigation of different physical aspects such as structural, mechanical, optical properties and Debye temperature of Fe_2ScM (M = P and As) semiconductors: A DFT-based first principles study, Int. J. Mod. Phys. B **32**, 1850121 (2018).

[54] S. Yalameha, Z. Nourbakhsh, and D. Vashaee, ElATools: A tool for analyzing anisotropic elastic properties of the 2D and 3D materials, Comput. Phys. Commun. **271**, 108195 (2022).

[55] F. Bernardini, V. Fiorentini, and D. Vanderbilt, Spontaneous polarization and piezoelectric constants of III-V nitrides, Phys. Rev. B **56**, R10024 (1997).

[56] T. Karaki, K. Yan, and M. Adachi, Subgrain microstructure in high-performance $BaTiO_3$ piezoelectric ceramics, Appl. Phys. Express **1**, 111402 (2008).

[57] W. Yue and J. Yi-Jian, Crystal orientation dependence of piezoelectric properties in $LiNbO_3$ and $LiTaO_3$, Opt. Mater. **23**, 403 (2003).

[58] I. B. Kobiakov, Elastic, piezoelectric and dielectric properties of ZnO and CdS single crystals in a wide range of temperatures, Solid State Commun. **35**, 305 (1980).

[59] T. Takenaka, H. Nagata, and Y. Hiruma, Current developments and prospective of lead-free piezoelectric ceramics, Jpn. J. Appl. Phys. **47**, 3787 (2008).